

Resolving the subsurface structure and elastic modulus of layered films via contact-resonance atomic force microscopy

Gheorghe Stan,^{1,*} Cristian V. Ciobanu,^{2,*} and Sean W. King³

¹ Material Measurement Laboratory, National Institute of Standards and Technology, Gaithersburg, Maryland 20899 USA

² Department of Mechanical Engineering and Materials Science Program, Colorado School of Mines, Golden, Colorado 80401, USA

³ Supplier Technology and Industry Development, Intel Corporation, Hillsboro, Oregon 97124, USA

Abstract. Since its discovery, atomic force microscopy (AFM) has become widely used for surface characterization, evolving from a tool for probing surface topography to a versatile method for characterizing mechanical, electrical, chemical, magnetic, and electro-optical properties of surfaces at the nanoscale. Developments of several AFM-based techniques have enabled even subsurface imaging, which is routinely being carried out at the qualitative level of feature detection for localized subsurface inhomogeneities. We surmise, however, that a quantitative 3D subsurface characterization can emerge from the AFM mechanical response of flat buried interfaces, and present here a methodology for determining the depth of a film and its mechanical properties. Using load-dependent contact resonance atomic force microscopy (CR-AFM) and accurate modeling of the contact between the AFM tip and a layered sample, we determine the relationship between the measured resonance frequency of the AFM probe and the contact stiffness. Our subsequent statistical analysis reveals an intrinsic and sample-specific interdependence between the depth and modulus sensitivities of CR-AFM. This interdependence prevents the simultaneous accurate determination of both depth and modulus from measurements on a single layered sample. If the elastic moduli of the sample components are pre-determined from separate investigations of bulk samples (or otherwise known), then this methodology accurately yields the location of the interface between the layers of the sample; as such, it can serve as a nondestructive and robust technique for probing layer thickness, subsurface features, and elastic properties of materials used in semiconductor electronics, additive manufacturing, or biomaterials.

Keywords: Contact-resonance atomic force microscopy, quantitative subsurface imaging, layered materials, correlative analysis, adhesive contact mechanics, finite element analysis

Corresponding authors' contact information: gheorghe.stan@nist.gov, cciobanu@mines.edu

Introduction

With the continuous decrease of physical dimensions in various exploratory scientific platforms and technological applications, nanoscale mechanical properties play an important role in the structure-functionality paradigm of materials design. Driven by semiconductor, battery and communication technologies, the 3D materials integration that sustains the deployment of ever smaller, faster, and more energy efficient devices requires non-destructive methods for characterizing mechanical properties that are critical for structural integrity, device functionality, material selection, and evaluation. Mechanical property measurements can be used along with other characterization techniques to expand our understanding of the morphology and properties of materials and to make advances in the fabrication of new materials and devices with desired properties and functionalities from nanoscale to macroscale.¹ Combining nanoscale mechanical and chemical characterizations, for example, has recently been used to reveal the nanoscale structure-property relationship of organosilicate materials with applications in electronics,²⁻⁴ and to examine morphological structures of cell walls,⁵ vesicles,⁶ and spores⁷ in biology.

Measurements that provide nanoscale mechanical property characterization emerge from various atomic force microscopy (AFM) techniques, with either quasi-static (force volume AFM)⁸ or dynamic operation (contact resonance AFM,⁹⁻¹⁰ ultrasonic AFM,¹¹ multi-frequency AFM,¹² bimodal AFM).¹³⁻¹⁴ They extract different mechanical properties of a material from observations of the response of a stimulated AFM tip-sample contact. Either in spectroscopic or mapping measurements, nanoscale mechanical AFM characterizations had been demonstrated on exposed surfaces of various materials and structures, including, for example, metals, ceramics, polymers, composites, films, nanostructures, and organics.^{4, 8, 15-18} In few instances,^{6, 19-21} it has been shown that some AFM methods can further provide a glimpse into the subsurface variation of mechanical properties of materials. In single frequency modulation techniques such as the contact resonance AFM (CR-AFM) and ultrasonic force microscopy (UFM) the subsurface contrast is due to changes of the deformation field underneath the sample surface.²² These changes are induced by the presence of material inhomogeneities in the matrix of the sample, e.g., particles,²³⁻²⁶ patterns,^{22, 27} or cavities,²⁸⁻³¹ leading to variations of the AFM tip-sample contact stiffness that are sensed as eigenmode frequency changes. In multi-frequency modulation techniques such as heterodyne force microscopy (HFM)³² and mode-synthesizing AFM (MSAFM),³³⁻³⁴ the subsurface contrast may originate from the scattering of the ultrasound waves guided through the sample; it has also

been pointed out³⁵⁻³⁶ that the ultrasound wavelengths are often orders of magnitude larger than the relevant dimensions of the subsurface features and their propagation through the sample would only marginally be altered.

In any AFM methods, the subsurface imaging via mechanical response stems from the ability to convert the observed contrast into quantitative characterization through modeling of mechanical interactions involved and the associated vibrational response. However, due to the complexity of the mechanics problem, the measured response has often been analyzed through approximate analytical models^{29, 37-38} or via simplified finite element analysis (FEA).²⁸ At times, the modeling of the AFM tip-sample system was done through a collection of springs and an equivalent stiffness for an inhomogeneous subsurface structure.³⁹ FEA calculations^{26, 28} could not always be used to accurately model the entire 3D response of the system due to the high computing power required to extract the elastic properties of subsurface features from the non-inverse analysis of the measurements. While approximate models and FEA calculations on simplified systems enable a rapid qualitative analysis (e.g., demonstrations of feature detection), their use can also obfuscate the strengths of the experimental technique and prevent the objective evaluation of its performance and limitations. Difficulties do not exclusively lie in the use of a model, as data collected from the vibrations of AFM tip-sample contact is noisy, and vibrational frequencies change with the load on the contact; averaging over many measurements at the same load, and performing measurements at different loads alleviate this problem, while adding complexity to the task. Attempting to resolve subsurface features by combining averaged AFM measurements with coarse or simplified models would lead to inaccurate characterization of the relevant dimensions or mechanical properties and hinder our understanding of the sensitivity and limitations of the method.

In this article, we present a method based on CR-AFM measurements and accurate modeling of the tip-sample contact to determine the depth and modulus of a flat interface in a layered sample. The CR-AFM observable is the frequency of an eigenmode of the cantilever when the AFM tip is loaded and in contact with the sample. This so-called contact resonance (CR) frequency directly relates to the tip-sample contact stiffness. We have performed load-dependent CR-AFM measurements⁴⁰ on a series of two-layer films to obtain the load dependence of the tip-sample contact stiffness. Unlike previous CR-AFM works based on single load measurements, we

demonstrate that eigenfrequency measurements and the associated contact stiffness under variable load, in correlation with physics-based mechanical models for the AFM tip-sample contact, provide the necessary means to describe the details of the mechanical response of the subsurface region. We have used physically faithful models of the tip-surface interaction in which the contact geometry, the sample material/structure, and the tip-sample interactions are input parameters in the mechanical modelling, which is realized in two independent ways. The first modeling framework is a set of semi-analytical equations⁴¹⁻⁴² that accurately reproduce the indentation of a spherical rigid on a half-space coated substrate in the presence of adhesion. The second way of modeling is 3D finite element analysis (FEA). Both frameworks have been used to predict the load-dependent contact stiffness for given layered structure of the sample, material, and tip-sample interaction and contact geometry. By comparing the contact stiffness resulted from the measured CR frequencies with those from the models, we evaluated the depth of the surface layer and its elastic properties. We have found that the elastic modulus sensitivity of CR-AFM increases with increasing layer thickness and the interface depth sensitivity increases with decreasing thickness. The two opposing trends explain why it is difficult to simultaneously resolve the material contrast and location of subsurface heterogeneities in nanomechanical subsurface imaging. However, through a quantitative analysis of the measurement uncertainties, we show that an optimal working point in the dual space of the correlated depth and elastic modulus parameters can be established for each structure. Furthermore, if either the elastic moduli of the layers or the depth of the interface is known or predetermined, then the remaining parameter can be accurately determined from our measurement uncertainty analysis. This methodology demonstrates that AFM-based subsurface mechanical characterization can be significantly improved, and its applicability further extended by means of quantitative analysis for probing layer thickness, subsurface features, and elastic properties of materials used in semiconductor electronics, additive manufacturing, or biomaterials.

Materials and Measurements

The low-k dielectric bilayer film structures investigated in this study are described in Figure 1, with the dimensions given in Table 1. These layered films were deposited on 300 mm diameter Si(001) substrates by plasma enhanced chemical vapor deposition (PECVD).⁴³ Briefly, the bottom SiOC:H low-k dielectric layer L₂ with a nominal thickness of 2000 nm was deposited by PECVD

using an alkoxy silane precursor diluted in an inert gas at a temperature on the order of 400 °C. The stiffer top layer, SiCO:H low-k dielectric (L_1 , with nominal thicknesses ranging from 10 to 500 nm) was deposited by PECVD using an organosilane and an oxidizing gas. The thicknesses of the two layers were independently determined using a spectroscopic ellipsometry based technique by individually depositing each film on a separate Si substrate. The properties of the two layers differ significantly from each other, due to their different mass densities (1.4 versus 2.0 g/cm³) and their different Si-C/Si-O network bond ratios (< 1.0 versus > 1.0).⁴⁴

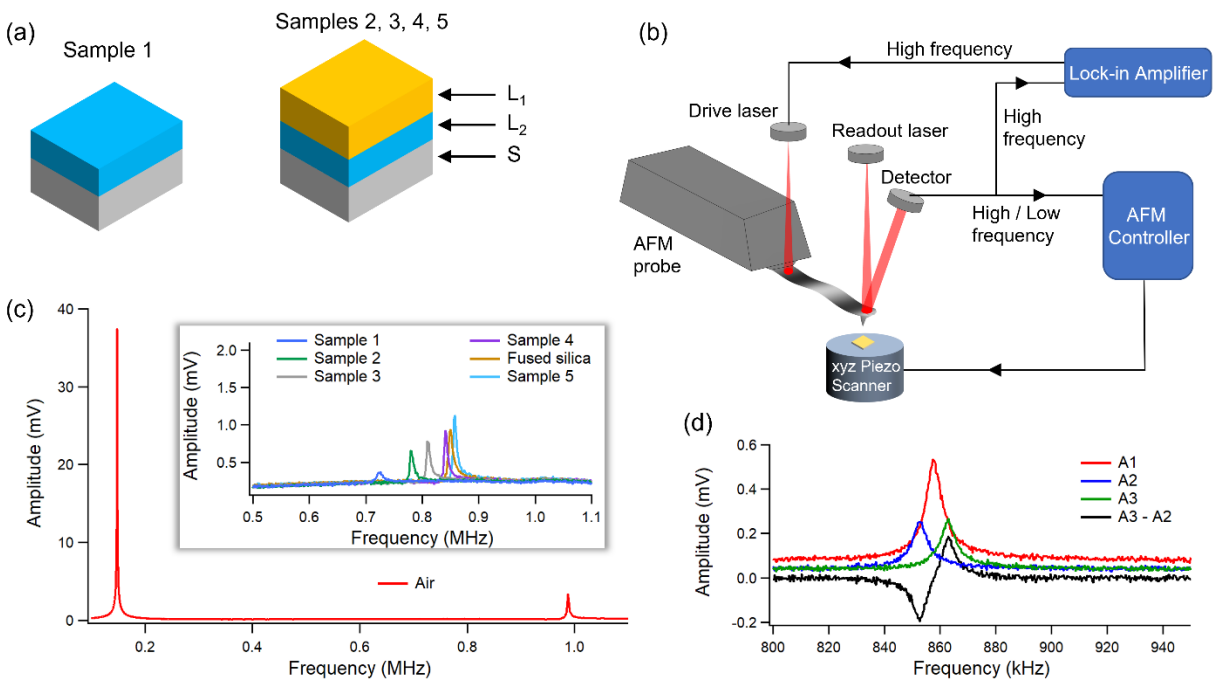


Figure 1: (a) The layered structure of the investigated samples consists of a top layer L_1 (yellow) and a bottom layer L_2 (blue) on a silicon substrate S (grey). Sample 1 has only the layer L_2 on the substrate S . (b) Schematic of the CR-AFM measurements with the modulation applied by a photothermal drive laser at the base of the cantilever. The applied and measured signals of the CR-AFM modulation are operated by a high-speed lock-in amplifier, while the tip-sample interaction was operated by the AFM controller. (c) Frequency sweep in air showing the first two flexural eigenmode peaks. Inset: frequency sweeps for the tip in contact with each of the samples and fused silica, under the same applied load of 150 nN. (d) Dual resonance frequency-tracking for the tip on fused silica, showing the main carrier A1 (red), the lower A2 (blue) and higher A3 (green) amplitude modulations bracketing the main carrier, and the difference A3-A2 (black) of the A3 and A2 modulations. A feedback control acts on the difference A3-A2 to follow any change in the CR frequency (see text for details).

Table 1: The layered structure of the samples measured. The bottom layer L_2 was SiOC:H and the top layer L_1 was SiCO:H. Their thicknesses were determined by spectroscopic ellipsometry of each individual layer deposited with its nominal thickness on the silicon substrate.

	Sample 1	Sample 2	Sample 3	Sample 4	Sample 5
L_1 thickness (nm)	none	9.1	20.8	105.7	476.9
L_2 thickness (nm)	2045.3	2043.5	2038.5	2026.5	2002.6

The CR-AFM measurements were performed on a MultiMode AFM (Bruker, Santa Barbara, California, USA) equipped with a custom-made optical head that incorporates a photothermal drive module.⁴⁵ The so-called “small cantilever head” was built during an open-science workshop at EPFL (Lausanne, Switzerland). The photothermal drive laser is mounted on an adjustable kinematic block; the positioning of its spot at the base of the cantilever is independent of that of the readout laser at the end of the cantilever. The CR-AFM oscillation was provided by the photothermal drive laser modulated by a small-amplitude, frequency-controlled signal from an UHF 600 MHz lock-in amplifier (Zurich Instruments AG, Zurich, Switzerland). To avoid the noise and bandwidth limitations of the AFM base’s electronics, the deflection signal from the readout detector was directly fed into the signal access module box of the AFM controller instead of being routed through the base of the AFM. The peak emission wavelengths of the readout and drive lasers of the photothermal head are around 645 nm and 686 nm, respectively.

Given that the materials in our study have elastic moduli from a few GPa to ≈ 100 GPa, the best sensitivity to the normal stiffness of the tip-sample contact in CR-AFM was accomplished by tracking the shift in the resonance frequency of the first eigenmode of the cantilever. The first two flexural eigenmode frequencies of the cantilever used (MikroMasch HQ:NSC14/Al BS, acquired from NanoAndMore USA Corp., Watsonville, CA, USA) were measured in air (out of contact) at 148.0 kHz and 987.4 kHz, respectively (Figure 1c). The stiffness of the cantilever was determined to be $7.2 \text{ N/m} \pm 0.2 \text{ N/m}$ from the thermal noise method integrated on the MultiMode AFM; the uncertainty represents one standard deviation of the mean value from 20 independent measurements. Once the AFM probe is brought into mechanical contact with a surface, all the eigenmode frequencies of the cantilever will undergo (positive) frequency shifts of their frequencies in accordance with the increased stiffness of the established tip-sample contact. Figure

1d shows frequency sweeps that include the resonance peaks of the first eigenmode in contact on each of the samples studied and fused silica; we used fused silica as a reference material with a well-known elastic modulus of 72 GPa. All the CR-AFM spectra shown in Figure 1d have been acquired under the same applied force of 150 nN and with the same tip. This means that the observed difference among the CR peaks is due to an intrinsic difference in the elastic properties of the samples and we can say that an increase in the elastic modulus is demonstrated as we go from Sample 1 to Sample 5; this is due to the increasing thickness of the stiffer layer L_1 .

In order to provide accurate probe-sample contact, we have imaged the AFM probe via scanning electron microscopy (SEM), and have used the dimensions measured from SEM images in constructing models of the tip for numerical FEA calculations. The SEM used was a Quanta 200 FEI (Portland, OR, USA). A detailed description of our measurement protocol and analysis is given at the beginning of the Supporting Information (SI).

Results and Discussion

CR-AFM frequency sweeps (e.g., Figure 1d) can be used to determine the CR frequency at a given applied force. Depending on the frequency range and the number of measurements to be acquired, these sweeps are relatively slow, each of the order of few seconds. In addition, the measurement of CR frequencies at different applied forces would be necessary to provide reliable data for the contact model used in analysis. To mitigate these aspects, the CR frequency can be continuously tracked under a variable load like in load-dependent CR-AFM⁴⁰ or intermittent CR-AFM (ICR-AFM).⁴⁶ CR frequency tracking is also commonly used in CR-AFM mapping under a fixed applied load. We have used the dual-frequency resonance-tracking (DFRT) method⁴⁷ on a UHF 600 MHz lock-in amplifier to perform load-dependent CR-AFM spectroscopy on each of the five samples and fused silica during regular force-distance AFM ramps; details of the DFRT measurements are presented in SI.

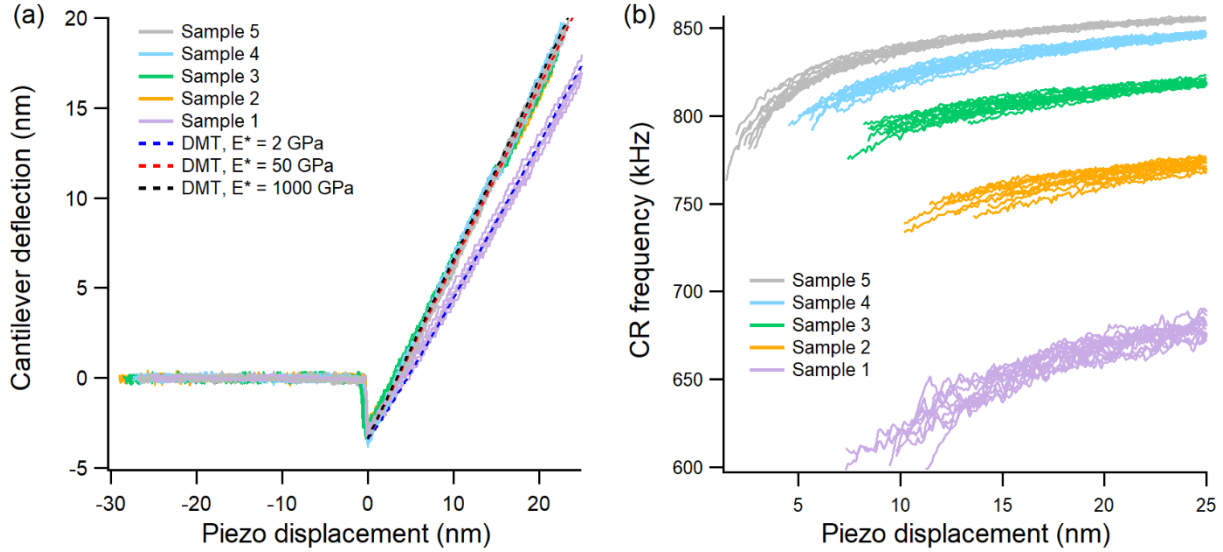


Figure 2: (a) Force-distance measurements (cantilever deflection versus piezo displacement) on Samples 1 through 5. The dashed lines are theoretical responses computed with the Derjaguin-Muller-Toporov (DMT) model for three hypothetical materials of different elastic moduli, going from 2 GPa (blue) to 50 GPa (red) and 1000 GPa (black). (b) Load-dependent CR-AFM measurements in the form of CR frequency versus piezo displacement.

Representative AFM force-distance curves from our measurements are shown in Figure 2a, where only five curves (out of 20) for each sample are plotted in order to avoid excessive overlap. There is only one set of the curves well separated from the rest, namely the curves corresponding to Sample 1. The smaller slope of the contact part of the curves measured on Sample 1 (Figure 2a) indicates that this sample is more compliant than Samples 2 – 5. However, there is practically no distinction among the contact parts of the curves for Samples 2, 3, 4, and 5, because within the range of small forces where usually the AFM is operated (here at forces smaller than 150 nN), the slope of the force-distance curves is less sensitive to the sample’s elastic modulus (few tens of GPa to hundreds of GPa). The lack of sensitivity of the force-distance curves to elastic modulus is also seen in theoretical models. Figure 2a shows theoretical cantilever deflections versus piezo displacements calculated for a few hypothetical elastic moduli of the sample; for moduli between 50 and 1000 GPa, there is no significant difference between the curves. These curves were computed based on the Derjaguin-Muller-Toporov (DMT) analytical model⁴⁸ that includes an adhesive force F_A outside the contact region in an otherwise Hertzian model.⁴⁹ The indentation depth d produced by a spherical rigid indenter into a half-space elastic material under an applied force F is given by⁴⁸

$$d = \left[\frac{3(F+F_A)}{4E^*\sqrt{R}} \right]^{2/3}, \quad (1)$$

where R is the tip radius and E^* is the reduced elastic modulus associated with the tip and sample. For a rigid tip, as the one considered here, $E^* = E/(1 - \nu^2)$, with E and ν being the Young's modulus and Poisson's ratio of the indented material.⁴⁹ The piezo displacement d_p is the sum of the indentation depth d and the cantilever deflections induced by the attractive adhesive force (F_A/k_c) and by the repulsive contact force (d_c),

$$d_p = d + F_A/k_c + d_c. \quad (2)$$

Both the measurements and theoretical curves shown in Figure 2a indicate that the force-distance curves cannot be used to differentiate between materials with elastic moduli larger than about 50 GPa. To achieve that differentiation, we resort to CR-AFM that directly relates the measured CR frequency to the stiffness of the tip-sample contact.

Figure 2b shows the load-dependent CR-AFM measurements along the contact parts of AFM force-distance curves performed on all the samples, about 15 curves for each sample (Figure S2 in SI, which includes measurements on fused silica). On each material, the DFRT method was used to lock-in on the CR frequency generated for cantilever deflections up to a maximum equivalent to 150 nN applied force. The central frequency and range for the DFRT were adjusted for each material, depending on its stiffness. All the force-distance ramps were made over 50 nm piezo displacement at a rate of 0.5 Hz per ramp. Figure 2b shows the measured CR frequencies as functions of the piezo displacement in the contact regime, going from zero to about 25 nm. In Figure 2b, we have shown only the acquisitions from the approach parts of the force-distance and CR frequency curves as the subsequent analysis will be focused only on them. In general, additional contributions from contact dissipation are observed on the retract parts.⁴⁰ The CR frequency was not acquired from the contact point on the most compliant materials (Samples 1 and Sample 2), rather, the optimized detection was performed for relatively strong contacts wherein the contact force was larger than the adhesion force. The best tracking for the CR frequency during contact loading was achieved for the stiffest material (Sample 5). Unlike the force-displacement curves (Figure 2a), Figure 2b shows excellent separation in terms of stiffness from sample to sample; furthermore, this separation of the curves holds for the entire range of applied force values considered. These load-dependent measurements offer the necessary profiles

to compare with semi-analytical or numerical calculations in order to extract the depth and elastic properties of the samples.

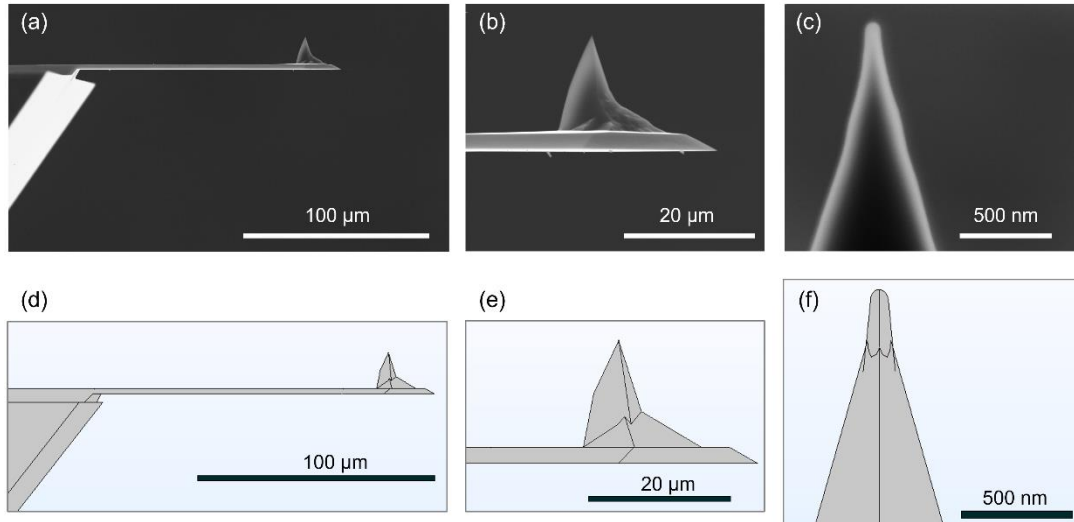


Figure 3: (a-c) SEM images of the AFM probe used to construct the geometry (shape and dimensions) of the AFM probe; the original scale bars of the SEM images are highlighted for clarity. (d-f) Counterparts of the SEM images (a-c) as modeled in COMSOL Multiphysics. The magnification and orientation chosen here provide clear view of the cantilever body and its connections to the base and tip and the apex of the tip cone.

The first step in correlating measurements and modeling consists in accurately converting the CR frequencies into contact stiffness. Such conversion requires a realistic geometric and mechanical description of the AFM probe, which includes the cantilever and the tip. In many CR-AFM analyses⁴ some of the geometrical parameters of the AFM probe (e.g., the tip radius and tip position along the cantilever) are not measured, and this information is instead bypassed by taking the ratio of successive measurements on the test sample and a reference material with known elastic modulus. Figures 3a-c display SEM images of the AFM probe at different magnifications (refer to Figures S3 and S4 in SI for the entire set of SEM images). From these images, we extracted the dimensions of the cantilever and tip and found them to be within less than 5 % percent of their nominal values provided by the manufacturer. It is worth pointing out that the AFM tip remained intact after the measurements, with a well-defined radius of 43 nm (Figure 3c).

The cantilever dynamics was modeled using the structural mechanics module of COMSOL Multiphysics 5.6 platform (COMSOL Inc., Burlington, MA, USA). The geometry used in the FEA calculations was based on the dimensions extracted from the SEM images of the AFM probe. A few of these COMSOL cantilever replicas are displayed in Figures 3d-f at 1:1 scale, for the exact orientations (also refer to Figures S3 and S4 in SI for side-by-side comparisons). Some of the geometric details that we have included in FEA –the underneath cut of the cantilever’s base (Figure 3a), the extent of the cantilever over the base (Figure S3 in SI), the trapezoidal cross-section of the cantilever (Figure S3), the pyramidal shape and orientation of the tip (Figure S4) are not captured by simple analytical models such as the Euler-Bernoulli beam theory.⁹ The precise tip location along the longitudinal axis of the cantilever (Figure 3a), as well as its lateral offset from the axis (Figure S4), are also factors that alter the dynamics of the cantilever. The entire AFM probe was tilted such that the cantilever’s plane makes an angle of 11° with respect to the horizontal xy plane of the surface of the sample, as in the actual AFM operation.

We have adopted a realistic description in the FEA modeling for the material of the AFM probe⁵⁰ (refer to SI). As specified by the vendor, the HQ:NSC14/Al BS AFM probes are made of silicon integrated probes with a backside aluminum coating of about 30 nm to increase reflectivity and a diamond-like carbon (DLC) coating on the tip side to increase the hardness of the tip. In COMSOL Multiphysics, we have used the fully anisotropic crystallography of silicon, with the surface of the AFM probe in the (100) plane and its axis along the [110] direction. The aluminum backside coating was neglected since we have checked that its contribution is negligible to the dynamics of the cantilever; the changes to the resonance frequencies of the cantilever due to this reflective coating is only few tens of Hertz. Since the DLC coating has significantly larger modulus than the samples probed, we took the tip to be fully rigid in FEA calculations and in the contact mechanics model (DMT).

The first two free (i.e., out of contact) resonance frequencies of the FEA-modeled AFM probe were computed to be 148.3 kHz and 988.5 kHz, respectively, which are within 1 kHz of their measured values. We have determined the cantilever stiffness from FEA calculations as follows. With direct vertical forces applied on the apex of the tip, the average vertical deflection of the tilted cantilever was measured over a circular region of 10 μm centered on the backside of the cantilever and located at the tip position (refer to Figure S6 in SI). This mimicked the actual

forces experienced by the tip during contact while the measured average deflection was similar to the real deflection of the cantilever determined from the four-quarter AFM photodetector. The stiffness of the cantilever, from FEA, was found to be 7.4 N/m, which is within 3 % of the average value measured by the thermal noise method.⁵¹ As both the stiffness and free flexural resonance frequencies of the FEA cantilever match closely the measured values, we conclude that the quasi-static and dynamic bending of the cantilever is very well reproduced by FEA, and the modeled AFM probe is suitable to also reproduce the cantilever mechanics when the tip is brought into contact.

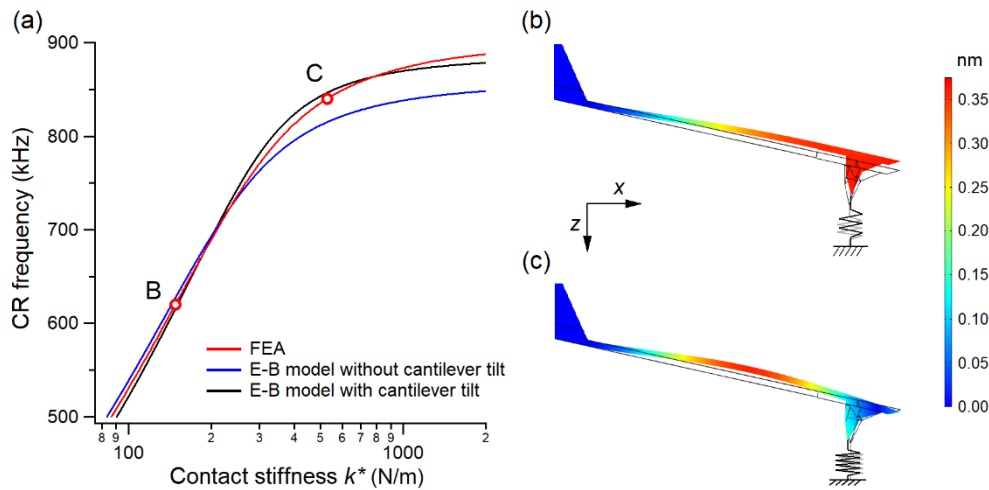


Figure 4: (a) First eigenmode resonance frequencies of the AFM probe as a function of the contact stiffness. Points B and C represent two tip-sample normal couplings, $k^* = 148$ N/m at $fc_1 = 620$ kHz (point B) and $k^* = 529$ N/m at $fc_1 = 840$ kHz (point C). The dependence of the contact resonance frequency on the contact stiffness has been calculated using FEA (red curve) based on the geometry of the AFM probe (Figure 3). For comparison, we have included predictions from the Euler-Bernoulli (E-B) beam theory, with black (blue) curves corresponding to the situation with (without) the cantilever tilt included. (b), (c) Shape of the cantilever’s vibrational profile corresponding to points B and C of panel (a), respectively. To highlight the shape differences for different contact stiffnesses, a scale factor of 10^4 was applied to the surface deformation.

Using FEA, we have converted our measured CR frequencies into contact stiffness values k^* (refer to Figure 4a). For making this conversion, in the FEA software we have attached springs with given spring constants at the end of the tip; these springs are oriented along the z direction in Figures 4b, c which would be perpendicular to the sample surface in experiments. Figures 4b, c

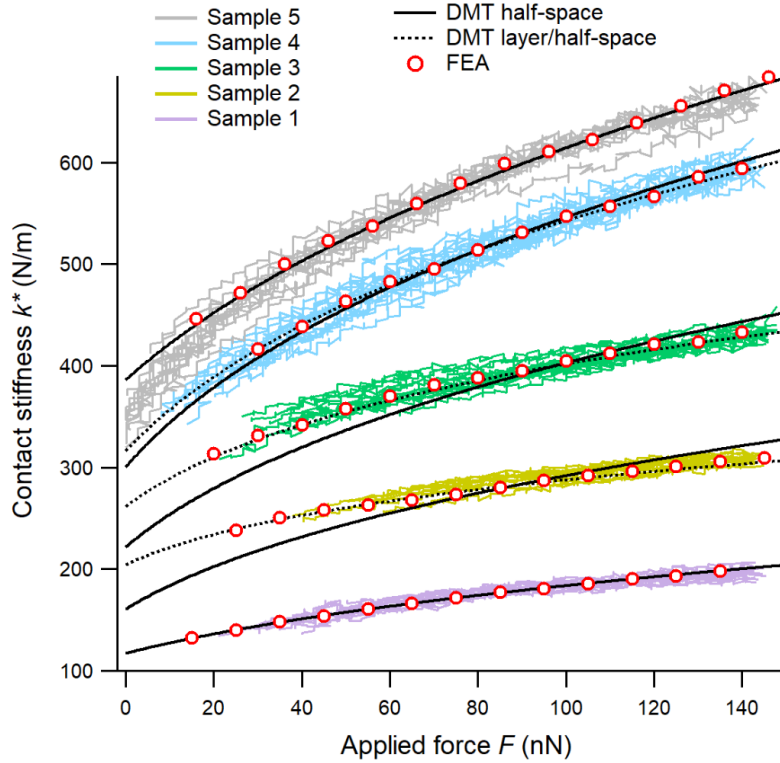


Figure 5: Contact stiffness versus applied force. The colored lines have been obtained from CR-AFM measurements on each of the samples. The black continuous lines are analytical DMT fits, considering each sample to be a homogeneous half-space of its top layer material. The dotted lines represent the semi-analytical DMT dependencies for nominal L_1 layer (Table 1) on L_2 half-spaces (i.e., large bottom-layer thickness limits for Samples 2 through 4). The red open circles represent data obtained from FEA calculations for each of the sample probed.

show two instances of the cantilever's bending corresponding to two different contact stiffnesses, with a larger deflection towards the end of the cantilever at lower k^* , and more bending in the middle of the cantilever at higher k^* . The CR frequency versus contact stiffness relationship calculated from FEA is shown in Figure 4a along with two theoretical dependences from the Euler-Bernoulli (E-B) beam theory, with and without cantilever tilt considered. The cantilever parameters needed for the two theoretical E-B functions were the same as those in FEA: cantilever length of $142.5 \mu\text{m}$, cantilever width of $33.4 \mu\text{m}$, cantilever thickness of $2.3 \mu\text{m}$, tip position at 0.86 from the base, tip height of $15 \mu\text{m}$, and cantilever tilt of 11° . For CR frequencies in the 600 kHz to 850 kHz range, the E-B model without the cantilever tilt substantially overestimates the contact stiffness, while the E-B model with cantilever tilt moderately underestimates the contact stiffness (Figure 4a). This analysis shows that separate FEA determination of the CR frequency

versus k^* curves is preferable to commonly used E-B models, even in the case where tilt is included.

The contact stiffnesses obtained from the measured CR frequencies and FEA modelling (Figure 4a) are plotted as functions of the applied force in Figure 5 for each sample. For a half-space Sample 1 (i.e., large L_2 thickness limit), half-space Sample 5 (large L_1 thickness limit), and fused silica (refer to Figure S9 in SI), we have used the analytical contact DMT model⁴⁸ to understand how well it describes the observed force dependence of the contact stiffness (continuous black curves in Figure 5) for one thick layer (L_1 or L_2) on a substrate. We have first tested the DMT model using the fused silica sample, for which we fit the average dependence of the converted contact stiffness versus applied force data by the DMT model, with using the tip radius and adhesive force as fit parameters. In this fit, the Young's modulus and Poisson's ratio for our test fused silica sample were taken as 72.0 GPa and 0.17. Within the 60 nN to 180 nN range of applied forces, the fit led to a tip radius of 42.6 nm and adhesive force of 35.6 nN. This tip radius value is in excellent agreement with the value determined directly from the SEM scans of the apex of the AFM probe. The adhesive force comes also close to the values observed in the pull-off force-distance contacts on the fused silica, which were in the 25 nN to 35 nN range. With the 43 nm value for the tip radius from the CR-AFM measurements on fused silica and from direct SEM measurements, the DMT analytical model was subsequently used to determine the elastic moduli of Sample 1 and Sample 5; the same Poisson's ratio of 0.2 was assumed for each of the sample. The fits resulted in Young's moduli of $12.8 \text{ GPa} \pm 0.3 \text{ GPa}$ and $78.9 \text{ GPa} \pm 3.0 \text{ GPa}$ for Sample 1 and Sample 5, respectively; the uncertainty represents one standard deviation from the mean value. We have used these moduli values for the subsequent analysis of Samples 2, 3, and 4.

To analyze the mechanics of the frictionless, adhesive contact between the tip (as a rigid indenter) and a multi-layer sample (Samples 2, 3, and 4), we have used a semi-analytical model⁴¹⁻⁴² which is also described in Sec. 6 of SI. Based on a transfer matrix method, the semi-analytical model reduces the stress-strain equations to two coupled integral equations for the stress distribution under the indenter and the ratio between the adhesion radius and the contact radius. The solution of these coupled equations⁴¹⁻⁴² are expressed in terms of load dependencies of the contact radius and indentation depth for various values of the adhesion parameter and layer

composition. These quantities can be used to calculate the contact stiffness, $k^* = \frac{\partial F}{\partial a}$, as a function of the applied force. Although the semi-analytical model⁴¹⁻⁴² considers a general Maugis-type adhesive interaction⁵² between the indenter and the contacted surface, we retained only the DMT limit of this interaction, with the adhesive force from force-distance curve measurements and the elastic moduli as determined above from the large thickness limits each layer. The results from the semi-analytical model (DMT for layer/half-space) are shown in Figure 5 with dotted lines for Samples 2 – 4. For these samples, we have also plotted the DMT half-space dependencies in Figure 5 (black lines); a comparative inspection reveals significant differences between the DMT layer/half-space model and DMT half-space. In the case of Sample 4, the difference between these two models, while observable, is less pronounced than for the other samples because the thickness of the top layer is large (~ 106 nm). This comparison suggests that in the regime of L_1 thicknesses corresponding to our samples, the layer geometry is important: the samples cannot be modeled as half-spaces unless L_1 thickness surpasses a certain threshold (that is greater than 106 nm, based on Figure 5). For each of Samples 2, 3, and 4, the average of the contact stiffness vs load curves (converted from the measured CR frequencies) is reproduced very well by the semi-analytical model, while visibly departing from the DMT half-space model. Notably, the results in Figure 5 indicate that CR-AFM can “sense” the $L_1 - L_2$ interface through a stiff coat (~ 80 GPa) that is at least 106 nm thick (Sample 4).

All the contact stiffness versus applied force measurements shown in Figure 5 were also determined from separate FEA calculations in COMSOL Multiphysics (details in SI), using a rigid tip, 78.9 GPa modulus for layer L_1 , and 12.8 GPa for layer L_2 , film dimensions from Table 1, 43 nm tip radius, and flat sample surface. The contact model of the FEA was frictionless and non-adhesive, and the contributions of the adhesive forces to the Hertzian FEA calculations were included by simply shifting the applied forces by the adhesive force measured on each material. The FEA calculations for the contact stiffnesses (open circles in Figure 5) are in excellent agreement with the DMT-layer/half-space dependences for Samples 2 through 5 (Figure 5). Such agreement suggests that the two methods can be used interchangeably for future quantitative investigations, based on considerations of computational time and complexity of the sample geometry.

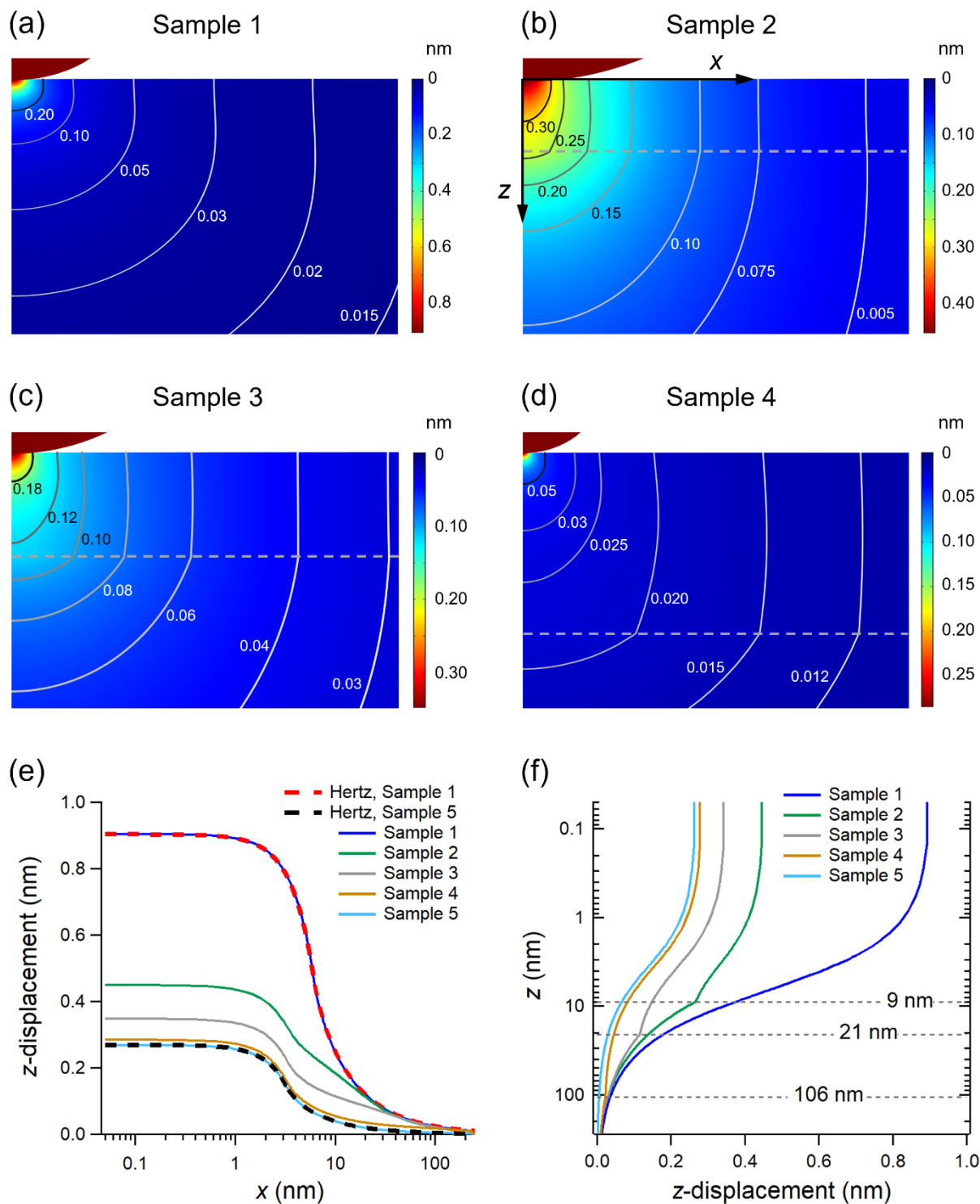


Figure 6: Displacement fields under the AFM tip at an applied vertical force of 100 nN. The cross sections shown are (a) $150 \text{ nm} \times 150 \text{ nm}$ of Sample 1; (b) $50 \text{ nm} \times 32 \text{ nm}$ of Sample 2; (c) $80 \text{ nm} \times 50 \text{ nm}$ of Sample 3; (d) $200 \text{ nm} \times 150 \text{ nm}$ of Sample 4. The selected contours, drawn at constant values of the z component of the displacement field, highlight the magnitude and spread of the deformation in the subsurface region

of each sample. The interface between the L_1 and L_2 layers (indicated by the dashed horizontal line in panels (b, c, d)) is located at 9 nm, 21 nm, and 106 nm below the surface of Sample 2, Sample 3, and Sample 4, respectively. (e, f) Profiles of the z -displacement along (e) the horizontal direction x at $z = 0$ and (f) the vertical direction z at $x = 0$, for all the samples, measured under 100 nN applied normal force. The dashed curves in (e) were calculated by using the Hertz contact model for half-space L_1 or L_2 materials. The kinks in (f) indicate the interface between the layers for Samples 2, 3, and 4.

We now focus on correlating the observed depth sensitivity of the CR-AFM measurements with the deformation field created in the subsurface region of each sample during indentation. Figures 6a through 6d show maps of the z -component of the displacement field in the xz plane of selected samples. Figures 6e and 6f display the z -deformation profiles along the x and z directions, respectively. For Sample 1 (in Figure 6a and 6e) and Sample 5 (in Figure 6f), the displacement field is radially smooth (no kinks) at any depth. In contrast, the displacement in each of the layered structures (Samples 2, 3, and 4) is noticeably perturbed or kinked at the interface between the two layers. The associated kinks are visible both in the cross-section maps (Figures 6b- d) and the vertical profiles in Figure 6f. Interestingly, the curves in Figure 6f start to align towards that of Sample 1 (same material as the bottom layer L_2) below the interface line. In general, noise in the measurements can greatly obfuscate the mechanical contrast of the subsurface inhomogeneities.⁵³ Below, we show that this contrast for a flat interface is quite achievable and well-resolved using CR-AFM down to depths of at least 106 nm through materials comparable in stiffness to fused silica.

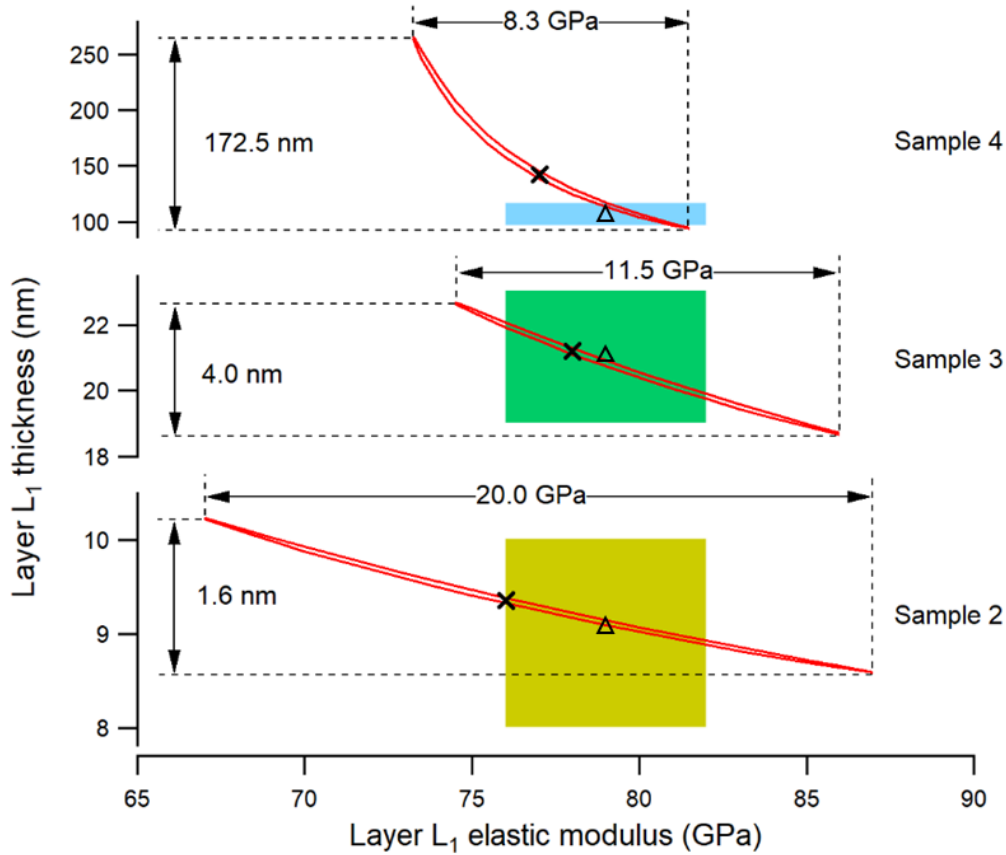


Figure 7. The red curves map the dual-uncertainty space of the thickness and elastic modulus of the layer L_1 (Samples 2, 3, and 4) calculated within 3 standard deviations of the best fits of the contact stiffness versus applied force measurements (Figure 5). An elastic modulus value of 12.8 GPa was taken for the L_2 layer of all samples. The crosses indicate the locations of the best fits for each of the three samples, and the open triangles indicate the nominal values of the thickness (Table 1) at the determined modulus. The rectangular boxes indicate the expected domain of values based on 10 % expected variations in nominal thickness and on the determined 79 ± 3 GPa L_1 modulus.

We now focus on investigating the quantitative limits of resolving the depth and the modulus of the top layer for the morphology of our samples, both presumed unknown at the outset. While the procedure is exemplified here for flat buried interfaces of layered structures analyzed via a semi-analytical (SI) model and FEA, it is also applicable to other geometries (e.g., buried nanoparticles or other subsurface inhomogeneities) that can be modeled only through FEA. We analyze the contact stiffness measurements (Figure 5) to find the best-fit values given by the semi-

analytical model⁴¹⁻⁴² for the thickness and elastic modulus of layer L₁. These two fit parameters are taken as free variables in the minimization of the goodness-of-fit⁵⁴ function χ^2 , defined as

$$\chi^2 = \sum_i^N \frac{(k_i^* - k_i^{*t})^2}{\sigma_i^2}, \quad (3)$$

where k_i^* are the contact stiffness (converted from CR frequencies) shown in Figure 5, k_i^{*t} are the theoretical contact stiffnesses calculated based on the DMT layer/half-space model, and σ_i is the standard deviation of the mean of the measurements in bin i ($1 \leq i \leq N$). For each sample, our data points corresponding to loads from 80 nN to 140 nN have been divided into $N = 24$ bins, each corresponding to a load increment of 2.5 nN. We included only the measurements for forces above 80 nN in order to avoid data scarcity at lower loads and to ensure a good measurement distribution for each sample. For a given sample and each bin i comprising M_i points, we have calculated the standard deviation of the mean as $\sigma_i = \sqrt{\sum_{j=1}^{M_i} (k_{i,j}^* - \langle k_i^* \rangle)^2 / (M_i(M_i - 1))}$; $\langle k_i^* \rangle$ is the mean of the M_i measurements $k_{i,j}^*$ ($1 \leq j \leq M_i$) in bin i . For the goodness-of-fit, we have retained χ^2 values within three standard deviations $3\sigma_{\chi^2} = 3\sqrt{2N}$ of its mean value N ; in our case, N was 24 and each M_i about 70. We have confirmed that the absolute minimum value χ_{\min}^2 of χ^2 , with respect to both fit parameters, was within $2\sigma_{\chi^2}$ of the mean, i.e. the null hypothesis test for N is satisfied. Figure 7 shows the contours of constant χ^2 at three standard deviations from the mean for Samples 2 – 4, and reveals different relationships between the two fit parameters in each case. The contours straddle the regions of the expected values for the two parameters (rectangular color boxes in Figure 7); these regions are defined based on an assumed, conservative 10 % uncertainty of the layer thickness and on the 79 ± 3 GPa elastic modulus of layer L₁ determined earlier in our analysis (Figure 5, DMT half-space analysis of Sample 5).

From Figure 7, we can see that for very thin layers (e.g., L₁ is about 9 nm for Sample 2) the fit is very sensitive to changes in thickness: variations of only 1.6 nm for the confidence region of L₁ thickness correspond to elastic modulus variations of 20 GPa. This illustrates a reduced modulus sensitivity and very good depth sensitivity for the CR-AFM-based subsurface imaging on very thin films for which both the depth and the elastic modulus are unknown. As the thickness of the layer L₁ increases (21 nm for Sample 2), the correlation between the two fit parameters (increased tilt of the χ^2 contours) increases, leading to a decrease in the thickness sensitivity and

increase in the elastic modulus sensitivity. For very thick layers (e.g., 106 nm for layer L₁ of Sample 4), the uncertainty in the elastic modulus, ± 4.2 GPa (Figure 7), approaches that of the measurements on the (nearly) half-space Sample 5 (Figure 5), ± 3 GPa, while the confidence limit for the layer thickness expands over a wide range (172.5 nm range, larger than the nominal layer thickness). This points to an inherent difficulty to simultaneously localize planar interfaces and accurately determine layer modulus. This is because the contact stiffness depends on both the dimensions and elastic modulus of the region probed; these dependences are coupled, leading to interdependent sensitivities of the stiffness with respect to depth and modulus. Although Figure 7 shows that uncertainties can be large (e.g., ± 86 nm for the layer thickness in Sample 4, or ± 10 GPa for the modulus in Sample 2), it is worth pointing out that the minimum χ^2_{\min} of the χ^2 function was found to be reasonably close to the expected values for both thickness and elastic modulus of the top layer for each of Samples 2 – 4. The above discussion considers the fit uncertainties if both fit parameters are unknown. However, if either the thickness or the elastic modulus is given or pre-determined, then this analysis will provide a very precise determination for the other parameter because the region enclosed within the χ^2 contours is very narrow for each sample (Figure 7). This means that for buried interfaces, we can either use their precise location to determine the material's modulus or, conversely, resolve the interface location underneath the surface based on knowledge of the elastic modulus.

Conclusion

To summarize, we have developed a quantitative methodology for resolving the layer thickness and elastic modulus of flat samples with layered morphologies. This methodology is based on a) load-dependent CR-AFM measurements on several layered samples, b) conversion of the measured resonance frequencies into contact stiffnesses using a faithful representation of the geometry and materials of the AFM probe in FEA calculations, and c) modeling of the tip-sample contact using either accurate FEA calculations or a semi-analytical DMT layer/half-space model. Our uncertainty analysis based on the goodness of fit parameter for the contact stiffness as a function of load (measured compared to modeled) has highlighted an inter-dependence of the depth and modulus sensitivities of the methodology: this interdependence prevents the simultaneous determination of interface depth and top layer elastic modulus from one single sample. We have

shown that the use of several samples results in the evaluation of the elastic moduli for the layer materials in the bulk limit. Although measurements on bulk samples may perhaps be seen as additional tasks that slow down the main characterization (e.g., when compared to faster methods focused mainly on subsurface feature detection) the large thickness limits for moduli are necessary inputs for the precise determination of layer thickness (interface depth). Our correlative analysis shows that the interplay between thickness and elastic modulus can be exploited to tune either the depth or material sensitivity of the CR-AFM based subsurface imaging; such tuning can prove useful for resolving mechanical effects based on interface or defect proximity, as well as for material or sample selection in various applications.

Disclaimer

Certain commercial equipment, software, instruments, and materials are identified in this document. Such identification does not imply recommendation or endorsement by the National Institute of Standards and Technology, nor does it imply that the products identified are necessarily the best available for the purpose.

ORCID iD

Gheorghe Stan - <https://orcid.org/0000-0001-5773-0328>

Cristian V. Ciobanu - <https://orcid.org/0000-0002-8476-4467>

Sean King - <https://orcid.org/0000-0001-5400-7679>

Supporting Information: Additional information on methodology, materials, and measurements (CR-AFM, dual-frequency resonance tracking), AFM contact geometry and probe materials, details of finite element analysis calculations in COMSOL Multiphysics, and equations of the contact model in the presence of adhesion.

Acknowledgment

The authors acknowledge the EPFL's Open Science Initiative (EPFL, Lausanne, Switzerland) and thank Professor Georg Fantner for his guidance and support in building the small cantilever AFM head.

References

- (1) Burnett, T. L.; Withers, P. J. Completing the Picture through Correlative Characterization. *Nature Materials* **2019**, *18* (10), 1041-1049.
- (2) Lo, M. K. F.; Dazzi, A.; Marcott, C. A.; Dillon, E.; Hu, Q. C.; Kjoller, K.; Prater, C. B.; King, S. W. Nanoscale Chemical-Mechanical Characterization of Nanoelectronic Low-K Dielectric/Cu Interconnects. *ECS Journal of Solid State Science and Technology* **2016**, *5* (4), P3018-P3024.
- (3) Stan, G.; Gates, R. S.; Hu, Q. C.; Kjoller, K.; Prater, C.; Singh, K. J.; Mays, E.; King, S. W. Relationships between Chemical Structure, Mechanical Properties and Materials Processing in Nanopatterned Organosilicate Fins. *Beilstein Journal of Nanotechnology* **2017**, *8*, 863-871.
- (4) Stan, G.; King, S. W. Atomic Force Microscopy for Nanoscale Mechanical Property Characterization. *Journal of Vacuum Science & Technology B* **2020**, *38* (6), 060801.
- (5) Tetard, L.; Passian, A.; Farahi, R. H.; Thundat, T.; Davison, B. H. Opto-Nanomechanical Spectroscopic Material Characterization. *Nature Nanotechnology* **2015**, *10* (10), 870-877.
- (6) Vitry, P.; Rebois, R.; Bourillot, E.; Deniset-Besseau, A.; Virolle, M. J.; Lesniewska, E.; Dazzi, A. Combining Infrared and Mode Synthesizing Atomic Force Microscopy: Application to the Study of Lipid Vesicles inside Streptomyces Bacteria. *Nano Research* **2016**, *9* (6), 1674-1681.
- (7) Rusciano, G.; Zito, G.; Isticato, R.; Sirec, T.; Ricca, E.; Bailo, E.; Sasso, A. Nanoscale Chemical Imaging of Bacillus Subtilis Spores by Combining Tip-Enhanced Raman Scattering and Advanced Statistical Tools. *ACS Nano* **2014**, *8* (12), 12300-12309.
- (8) Butt, H. J.; Cappella, B.; Kappl, M. Force Measurements with the Atomic Force Microscope: Technique, Interpretation and Applications. *Surface Science Reports* **2005**, *59* (1-6), 1-152.
- (9) Rabe, U.; Janser, K.; Arnold, W. Vibrations of Free and Surface-Coupled Atomic Force Microscope Cantilevers: Theory and Experiment. *Review of Scientific Instruments* **1996**, *67* (9), 3281-3293.
- (10) Yamanaka, K.; Nakano, S. Ultrasonic Atomic Force Microscope with Overtone Excitation of Cantilever. *Japanese Journal of Applied Physics Part 1-Regular Papers Short Notes & Review Papers* **1996**, *35* (6B), 3787-3792.
- (11) Yamanaka, K.; Ogiso, H.; Kolosov, O. Ultrasonic Force Microscopy for Nanometer Resolution Subsurface Imaging. *Applied Physics Letters* **1994**, *64* (2), 178-180.
- (12) Garcia, R.; Herruzo, E. T. The Emergence of Multifrequency Force Microscopy. *Nature Nanotechnology* **2012**, *7* (4), 217-226.

- (13) Rodriguez, T. R.; Garcia, R. Compositional Mapping of Surfaces in Atomic Force Microscopy by Excitation of the Second Normal Mode of the Microcantilever. *Applied Physics Letters* **2004**, *84* (3), 449-451.
- (14) Proksch, R. Multifrequency, Repulsive-Mode Amplitude-Modulated Atomic Force Microscopy. *Applied Physics Letters* **2006**, *89* (11), 113121.
- (15) Garcia, R.; Magerle, R.; Perez, R. Nanoscale Compositional Mapping with Gentle Forces. *Nature Materials* **2007**, *6* (6), 405-411.
- (16) Young, T. J.; Monclus, M. A.; Burnett, T. L.; Broughton, W. R.; Ogin, S. L.; Smith, P. A. The Use of the Peakforce (Tm) Quantitative Nanomechanical Mapping Afm-Based Method for High-Resolution Young's Modulus Measurement of Polymers. *Measurement Science and Technology* **2011**, *22* (12), 125703.
- (17) Garcia, R. Nanomechanical Mapping of Soft Materials with the Atomic Force Microscope: Methods, Theory and Applications. *Chemical Society Reviews* **2020**, *49* (16), 5850-5884.
- (18) Cross, S. E.; Jin, Y. S.; Rao, J.; Gimzewski, J. K. Nanomechanical Analysis of Cells from Cancer Patients. *Nature Nanotechnology* **2007**, *2* (12), 780-783.
- (19) Shekhawat, G. S.; Dravid, V. P. Nanoscale Imaging of Buried Structures Via Scanning near-Field Ultrasound Holography. *Science* **2005**, *310* (5745), 89-92.
- (20) Tetard, L.; Passian, A.; Venmar, K. T.; Lynch, R. M.; Voy, B. H.; Shekhawat, G.; Dravid, V. P.; Thundat, T. Imaging Nanoparticles in Cells by Nanomechanical Holography. *Nature Nanotechnology* **2008**, *3* (8), 501-505.
- (21) Stan, G.; Mays, E.; Yoo, H. J.; King, S. W. Nanoscale Tomographic Reconstruction of the Subsurface Mechanical Properties of Low-K High-Aspect Ratio Patterns. *Nanotechnology* **2016**, *27* (48), 485706.
- (22) van Es, M. H.; Mohtashami, A.; Thijssen, R. M. T.; Piras, D.; van Neer, P.; Sadeghian, H. Mapping Buried Nanostructures Using Subsurface Ultrasonic Resonance Force Microscopy. *Ultramicroscopy* **2018**, *184*, 209-216.
- (23) Killgore, J. P.; Kelly, J. Y.; Stafford, C. M.; Fasolka, M. J.; Hurley, D. C. Quantitative Subsurface Contact Resonance Force Microscopy of Model Polymer Nanocomposites. *Nanotechnology* **2011**, *22* (17), 175706.
- (24) Kimura, K.; Kobayashi, K.; Matsushige, K.; Yamada, H. Imaging of Au Nanoparticles Deeply Buried in Polymer Matrix by Various Atomic Force Microscopy Techniques. *Ultramicroscopy* **2013**, *133*, 41-49.
- (25) Ebeling, D.; Eslami, B.; Solares, S. D. Visualizing the Subsurface of Soft Matter: Simultaneous Topographical Imaging, Depth Modulation, and Compositional Mapping with Triple Frequency Atomic Force Microscopy. *ACS Nano* **2013**, *7* (11), 10387-10396.
- (26) Hennes, M.; Jakob, A. M.; Lehnert, F.; Ross, U.; Lotnyk, A.; Mayr, S. G. Nanometer-Resolved Quantification of Mechanical Response in Nanoparticle-Based Composites. *Nanoscale* **2016**, *8* (17), 9398-9404.
- (27) Wang, W. T.; Ma, C. F.; Chen, Y. H.; Zheng, L.; Liu, H. R.; Chu, J. R. Subsurface Imaging of Flexible Circuits Via Contact Resonance Atomic Force Microscopy. *Beilstein Journal of Nanotechnology* **2019**, *10*, 1636-1647.
- (28) Parlak, Z.; Degertekin, F. L. Contact Stiffness of Finite Size Subsurface Defects for Atomic Force Microscopy: Three-Dimensional Finite Element Modeling and Experimental Verification. *Journal of Applied Physics* **2008**, *103* (11), 114910.

- (29) Striegler, A.; Koehler, B.; Bendjus, B.; Roellig, M.; Kopycinska-Mueller, M.; Meyendorf, N. Detection of Buried Reference Structures by Use of Atomic Force Acoustic Microscopy. *Ultramicroscopy* **2011**, *111* (8), 1405-1416.
- (30) Ma, C. F.; Chen, Y. H.; Arnold, W.; Chu, J. R. Detection of Subsurface Cavity Structures Using Contact-Resonance Atomic Force Microscopy. *Journal of Applied Physics* **2017**, *121* (15), 154301.
- (31) Yip, K.; Cui, T.; Sun, Y.; Filleter, T. Investigating the Detection Limit of Subsurface Holes under Graphite with Atomic Force Acoustic Microscopy. *Nanoscale* **2019**, *11* (22), 10961-10967.
- (32) Cuberes, M. T.; Assender, H. E.; Briggs, G. A. D.; Kolosov, O. V. Heterodyne Force Microscopy of Pmma/Rubber Nanocomposites: Nanomapping of Viscoelastic Response at Ultrasonic Frequencies. *Journal of Physics D-Applied Physics* **2000**, *33* (19), 2347-2355.
- (33) Tetard, L.; Passian, A.; Thundat, T. New Modes for Subsurface Atomic Force Microscopy through Nanomechanical Coupling. *Nature Nanotechnology* **2010**, *5* (2), 105-109.
- (34) Vitry, P.; Bourillot, E.; Plassard, C.; Lacroute, Y.; Tetard, L.; Lesniewska, E. Advances in Quantitative Nanoscale Subsurface Imaging by Mode-Synthesizing Atomic Force Microscopy. *Applied Physics Letters* **2014**, *105* (5), 053110.
- (35) Ma, C. F.; Arnold, W. Nanoscale Ultrasonic Subsurface Imaging with Atomic Force Microscopy. *Journal of Applied Physics* **2020**, *128* (18), 180901.
- (36) Verbiest, G. J.; Simon, J. N.; Oosterkamp, T. H.; Rost, M. J. Subsurface Atomic Force Microscopy: Towards a Quantitative Understanding. *Nanotechnology* **2012**, *23* (14), 145704.
- (37) Sarioglu, A. F.; Atalar, A.; Degertekin, F. L. Modeling the Effect of Subsurface Interface Defects on Contact Stiffness for Ultrasonic Atomic Force Microscopy. *Applied Physics Letters* **2004**, *84* (26), 5368-5370.
- (38) Gisbert, V. G.; Garcia, R. Accurate Wide-Modulus-Range Nanomechanical Mapping of Ultrathin Interfaces with Bimodal Atomic Force Microscopy. *ACS Nano* **2021**, *15* (12), 20574-20581.
- (39) Ma, C.; Wang, W.; Chen, Y.; Arnold, W.; Chu, J. Depth-Sensing Using Afm Contact-Resonance Imaging and Spectroscopy at the Nanoscale. *Journal of Applied Physics* **2019**, *126* (12), 124302.
- (40) Stan, G.; Solares, S. D.; Pittenger, B.; Erina, N.; Su, C. M. Nanoscale Mechanics by Tomographic Contact Resonance Atomic Force Microscopy. *Nanoscale* **2014**, *6* (2), 962-969.
- (41) Sergici, A. O.; Adams, G. G.; Muftu, S. Adhesion in the Contact of a Spherical Indenter with a Layered Elastic Half-Space. *Journal of the Mechanics and Physics of Solids* **2006**, *54* (9), 1843-1861.
- (42) Stan, G.; Adams, G. G. Adhesive Contact between a Rigid Spherical Indenter and an Elastic Multi-Layer Coated Substrate. *International Journal of Solids and Structures* **2016**, *87*, 1-10.
- (43) Chen, J. W.; King, S. W.; Muthuswamy, E.; Koryttseva, A.; Wu, D.; Navrotsky, A. Thermodynamic Stability of Low-K Amorphous Sioc Dielectric Films. *Journal of the American Ceramic Society* **2016**, *99* (8), 2752-2759.
- (44) Pomorski, T. A.; Bittel, B. C.; Lenahan, P. M.; Mays, E.; Ege, C.; Bielefeld, J.; Michalak, D.; King, S. W. Defect Structure and Electronic Properties of Sioc:H Films Used for Back End of Line Dielectrics. *Journal of Applied Physics* **2014**, *115* (23), 234508.
- (45) Nievergelt, A. P.; Adams, J. D.; Odermatt, P. D.; Fantner, G. E. High-Frequency Multimodal Atomic Force Microscopy. *Beilstein Journal of Nanotechnology* **2014**, *5*, 2459-2467.

- (46) Stan, G.; Gates, R. S. Intermittent Contact Resonance Atomic Force Microscopy. *Nanotechnology* **2014**, *25* (24), 245702.
- (47) Rodriguez, B. J.; Callahan, C.; Kalinin, S. V.; Proksch, R. Dual-Frequency Resonance-Tracking Atomic Force Microscopy. *Nanotechnology* **2007**, *18* (47), 475504.
- (48) Derjaguin, B. V.; Muller, V. M.; Toporov, Y. P. Effect of Contact Deformations on the Adhesion of Particles. *Journal of Colloid and Interface Science* **1975**, *53* (2), 314-326.
- (49) Johnson, K. L., *Contact Mechanics*. Cambridge University Press: Cambridge, 1985; pp 84-106.
- (50) Hopcroft, M. A.; Nix, W. D.; Kenny, T. W. What Is the Young's Modulus of Silicon? *Journal of Microelectromechanical Systems* **2010**, *19* (2), 229-238.
- (51) Hutter, J. L.; Bechhoefer, J. Calibration of Atomic-Force Microscope Tips. *Review of Scientific Instruments* **1993**, *64* (7), 1868-1873.
- (52) Maugis, D. Adhesion of Spheres: The J K R-D M T Transition Using a Dugdale Model. *Journal of Colloid and Interface Science* **1992**, *150* (1), 243-269.
- (53) Malavé, V.; Killgore, J. P.; Garboczi, E. J. Decoupling Subsurface Inhomogeneities: A 3d Finite Element Approach for Contact Nanomechanical Measurements. *Nanotechnology* **2019**, *30* (28), 285703.
- (54) Hughes, I. G.; Hase, T. P. A., *Measurements and Their Uncertainties: A Practical Guide to Modern Error Analysis*. Oxford University Press: Cambridge, 2010; pp 67-84.

TOC GRAPHICS

